nature communications

Article

https://doi.org/10.1038/s41467-026-69901-3

Topology optimization of thermoelectric generator for maximum power efficiency

Received: 10 December 2025

Accepted: 10 February 2026

Published online: 19 February 2026

Check for updates

Jungsoo Lee[1,2,3,5], Seong Eun Yang[1,5], Seungjun Choo[1,5], Haiyang Li[1], Hyunjin Han[1], Keonkuk Kim[1], Yae Eun Park[1], Ho Hyeong Lee[4], Dong-Woo Suh[4], Hayoung Chung[2] ✉ & Jae Sung Son[1] ✉

Thermoelectric generators offer a promising approach for harvesting waste heat from both natural and human-made sources, enabling sustainable electricity generation. While geometric design plays a crucial role in optimizing device performance, conventional approaches remain confined to simple configurations, limiting efficiency improvements. This constraint arises from the complex interplay of multiphysical interactions and diverse thermal environments, which complicates structural optimization. Here, we introduce a universal design framework that integrates topology optimization (TO) with additive manufacturing to systematically derive high-efficiency thermoelectric 3D architectures. By formulating an optimization problem to maximize power generation efficiency, our approach explores an unprecedentedly large design space, optimizing the geometries of thermoelectric materials across diverse thermal boundary conditions and material properties. The resulting TO-derived geometries consistently outperform conventional cuboids, demonstrating significant efficiency gains. Beyond in-silico studies, we provide theoretical insights and experimental validation, confirming the feasibility of our design approach. Our study offers a transformative way for enhancing thermoelectric power generation, with broad implications for next-generation sustainable energy technologies.

Geometry plays a fundamental role in functional performance in both natural and engineered systems. In nature, evolutionary processes have shaped optimized architectures that exhibit exceptional properties. For instance, nacre in mollusk shells balances strength and toughness through its layered structures[1], while gecko footpads feature microscopic geometries that enhance adhesion via van der Waals forces[2]. Similarly, geometric design is equally critical in materials engineering, where structural functionalities are often optimized through shape modifications. Examples include lattice architectures for mechanical stiffness[3], photonic crystals for light manipulation[4], and heat sink designs for thermal management[5]. Despite its significance, however, geometry is often overlooked in engineering design, which traditionally relies on empirical heuristics or trial-and-error methods—an approach that limits the exploration of unconventional yet efficient geometries. Recently, topology optimization (TO) fundamentally challenges this oversight by systematically generating geometries that maximize performance beyond conventional design constraints[6]. Unlike the traditional approach, which adjusts a few predefined dimensions within a fixed connectivity, TO formulates design as a material-distribution problem over the entire domain. TO has been

[1]Department of Chemical Engineering, Pohang University of Science and Technology (POSTECH), Gyeongsangbuk-do, Republic of Korea. [2]Department of Mechanical Engineering, Ulsan National Institute of Science and Technology, Ulsan, South Korea. [3]KAIST InnoCORE PRISM-AI Center, Korea Advanced Institute of Science and Technology (KAIST), Daejeon, Republic of Korea. [4]Graduate Institute of Ferrous & Eco Materials Technology, Pohang University of Science and Technology, Pohang, Republic of Korea. [5]These authors contributed equally: Jungsoo Lee, Seong Eun Yang, Seungjun Choo.
✉e-mail: hychung@unist.ac.kr; sonjs@postech.ac.kr

reported to explore a vastly larger, high-dimensional search space—ranging from thousands to millions of effective design variables, uncovering non-intuitive layouts unattainable to low-dimensional parametric methods[7]. This approach has demonstrated success across aerospace[8], automotive[9], and materials science[10]. When combined with advanced manufacturing techniques such as three-dimensional (3D) printing.[11–13], TO further expand design possibilities and facilitate the fabrication of complex, high-performance structures that were previously impractical or impossible.

Thermoelectric (TE) energy conversion has drawn significant attention due to its ability to directly convert heat into electricity, offering a sustainable approach to harvesting waste heat from natural and human-made sources, including residential, industrial, and transportation systems[14–18]. Like many other engineering systems, TE generators (TEGs) demonstrate the importance of geometric design, as their performance can be enhanced not only through material advancements but also through the change of their geometry[19–24]. Properly engineered TE material geometries within a TEG can optimize heat flow, enhance thermal gradients, and improve electrical output, ultimately leading to substantial performance gains. However, the inherent complexity of TE systems—stemming from the intricate interplay between thermal and electrical transport, as well as varying thermal environments— presents significant design challenges[25–27]. Current design strategies, which rely predominantly on empirical knowledge and heuristic-based modifications, remain confined to a narrow design space, resulting in simple shapes and topologies with limited performance improvements.

Here, we introduce a TO framework for the design of TE materials aimed at maximizing power generation efficiency. As illustrated in Fig. 1, our methodology employs finite element-based TO to generate geometries that align with specified objective functions by incorporating system parameters as inputs. This framework handles thousands to tens of thousands of design variables, providing almost limitless degrees of freedom in geometric designs. Such resolution lets the algorithm add, remove or relocate material anywhere in the domain automatically and intelligently, generating "real" optimum designs that satisfy device constraints in the real environments—boundary conditions, interfacial resistances, temperature-dependent properties, packaging limits, and mechanical stresses—in a single loop. Compared to cuboidal TEGs, the optimized geometries consistently exhibit superior power generation performances across all tested boundary conditions and materials, achieving enhancements of up to eightfold. The experimental results obtained from 3D-printed materials closely aligned with computational predictions, confirming the validity and feasibility of our approach. These findings establish TO as a powerful platform for designing high-performance TE devices with broad applicability in real-world energy harvesting systems.

Results

Optimums with different thermal boundaries

We applied TO on a single-leg TEG sandwiched between top and bottom copper electrodes to derive optimal leg geometries that maximize power generation efficiency (η). The overall optimization process is illustrated in Fig. 1b. Extrinsic thermal boundary conditions are a crucial factor influencing the overall power generation performance of a device[19,28–30]. Accordingly, we optimized the previously reported 3D-printed BiSbTe model material under various boundary conditions, incorporating convection, heat flux, and temperature (Fig. 2 and Supplementary Fig. 1)[31]. Initially, optimization was conducted under convective heating and cooling, with the convection coefficient (h) varied from 10 to 1000 W m^{-2} K^{-1} (Fig. 2a and Supplementary Fig. 2), covering the wide range of thermal environments encountered in TEGs. The optimized geometries exhibit broadly similar features, primarily adopting an I-shape. Under all conditions, the optimal geometries achieved higher η than both the initial model and the cuboidal models of equivalent volume. As h decreased on both sides, the refined

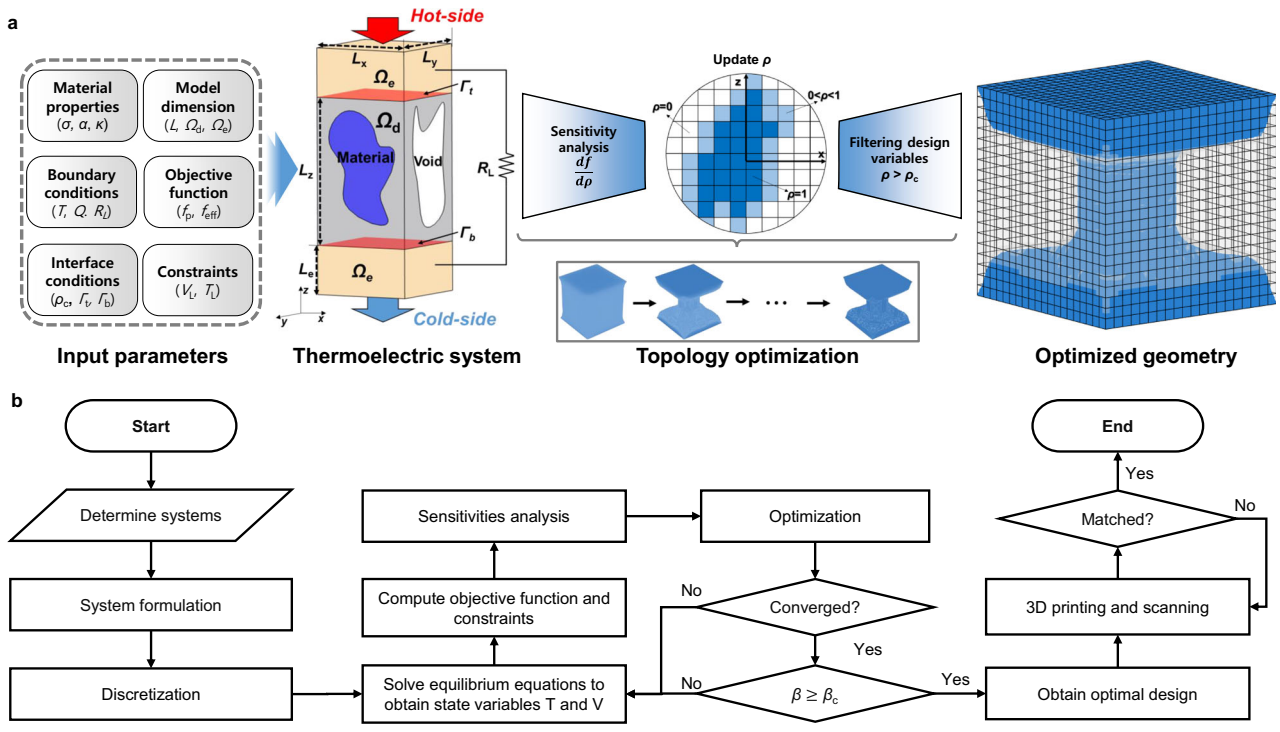

Fig. 1 | Overview of the TO process for TE materials. a Schematic depiction of the TO process, illustrating how the optimal layout of TE materials is determined under various system parameters. The layout is optimized by maximizing the objective function (P or η) defined within the TE power generation system. **b** Flowchart summarizing the sequential steps of the TO process for TE materials. In this flowchart, T represents temperature, V denotes voltage, β indicates the projection slope, and β_c is the predefined threshold value.

https://doi.org/10.1038/s41467-026-69901-3

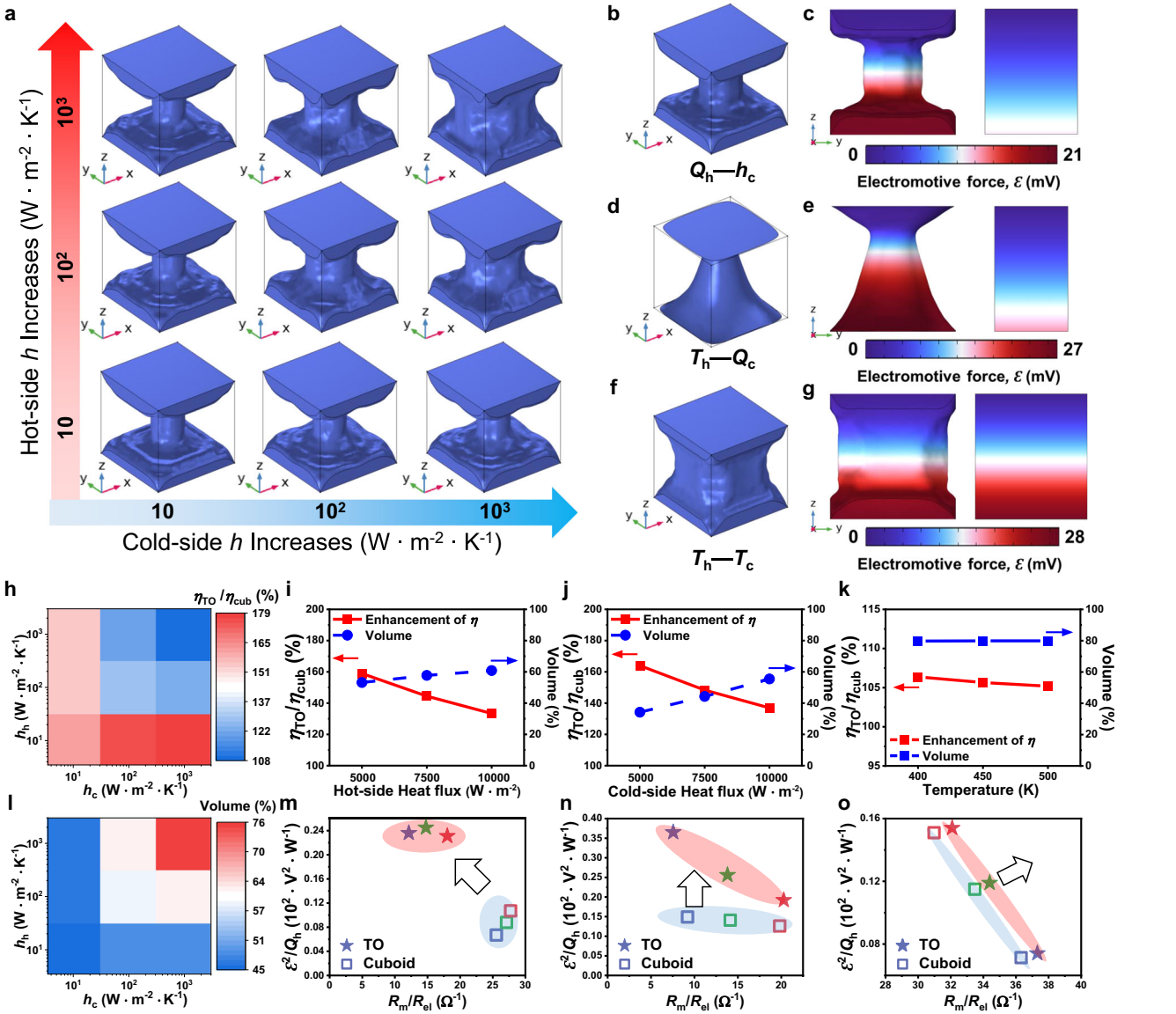

Fig. 2 | Optimums with different thermal boundaries. Optimized BiSbTe geometries for (**a**) convective cooling and heating conditions with h of $10–10^3\,W\,m^{-2}\,K^{-1}$; (**b**) fixed Q_h and convective cooling; (**d**) fixed T_h and Q_c; and (**f**) fixed temperature boundaries on both sides. Comparison of the electromotive force distributions for each optimized geometry (left) and a reference cuboid with the same material volume (right), corresponding to **b (c), d (e)**, and **f (g)**, respectively. h–l, η enhancement compared to a reference cuboid of the same volume, together with the volume fraction of the optimized geometry as a percentage of the total design domain. Results from **a** are shown in (**h**, **l**), from **b** in (**i**), from **d** in (**j**), and from **f** in (**k**). Analysis of the η enhancement achieved through optimal design from **b** (**m**), from **c** (**n**), from **d** (**o**). Blue represents the lowest heat or temperature, green intermediate values, and red the highest, whereas star symbols mark the optimized designs and hollow squares denote the reference cuboid. $\mathscr{E}^2/Q_h$ indicates the conversion factor, and R_m/R_{el} denotes the matching conductance. Shaded zones highlight trends for the optimized and cuboid geometries.

geometric features became thinner, and the overall relative volume of the optimized geometry gradually decreased—resulting in a larger enhancement in η relative to cuboidal models. The maximum η enhancement of 79% was observed under the strongest cooling and weakest heating conditions (Fig. 2h, l). This enhancement was amplified under extreme operating conditions (Supplementary Fig. 3). Under same boundary conditions, power optimization exhibited the same tendency—favoring thicker geometries than η optimization—and yielded up to a 59% increase in output power (Supplementary Figs. 4 and 5).

To better reflect heat transfer conditions commonly encountered in industrial and practical engineering applications, we further applied the TO process under three specific boundary conditions. First, we considered a fixed heat-flux (Q_h) combined with convective cooling (Fig. 2b, c and Supplementary Fig. 6). This boundary condition is widely recognized as the most common thermal environment in practical applications, particularly when a TEG is applied to heat sources, with the cold side being cooled via passive or active cooling mechanisms[32–35]. Similar to the case under convective heating and cooling, the optimized geometries exhibit pronounced lateral trimming, yielding an I-shape. As the Q_h decreases, the refined geometric features become thinner while the overall volume gradually contracts. At the Q_h of $5000\,W\,m^{-2}$, the optimized geometry achieves ~59% enhancement in η compared to a cuboid (Fig. 2i).

As the second condition, we examined the cases where the hot-side temperature (T_h) is fixed, and a constant heat flux (Q_c) is applied at the cold side. This setup represents the operating condition of a hot reservoir with systemized cooling[32,36]. Under these conditions, the

optimal geometry takes the form of an asymmetric hourglass, with a greater proportion of material near the lower part (Fig. 2d, e and Supplementary Fig. 6). Each optimized design is cooled to the preset temperature limit (Supplementary Fig. 7), indicating that the TE material adopts an hourglass to maximize temperature difference (ΔT). The asymmetry between the top-and bottom-layout likely results from the redistribution of material to the lower-temperature region, where the material exhibits a high figure-of-merit (ZT). As the Q_c increases, the optimal geometry requires a larger material volume. At the Q_c of 5000 W m^{-2}, the optimized geometry achieves ~64% enhancement in η compared to a cuboid (Fig. 2j).

The third boundary condition we investigated involves fixing both hot-side and cold-side temperatures (T_c) (Fixed-T conditions). This setup is widely used in laboratory experiments to evaluate the power generation of TEGs. However, it assumes continuous and infinite heat transfer at both junctions, making it relevant only to idealized scenarios such as hot and cold reservoirs[19,37–39]. Under this condition, the optimized design maximizes the contact area with electrodes while maintaining the material volume below the preset maximum, resulting in only minimal side-surface trimming (Fig. 2f, g and Supplementary Fig. 6). This small geometric change is expected because the fixed-temperature boundary inherently determines the ΔT and the resulting electromotive force ($\mathscr{E}$) of the TE legs, leaving little room for optimization. Nonetheless, compared to a cuboid, the optimized geometries still achieve up to a 6% enhancement in η, primarily due to higher thermal resistance (R_{th}), which reduces the required heat flux Q_h (Fig. 2k).

Fundamentally, the device η is determined by the conversion factor ($\mathscr{E}^2/Q_h$) and the matching conductance (R_m/R_{el}),

$$\eta = \frac{\mathscr{E}^2}{Q_h}\frac{R_m}{R_{el}} \tag{1}$$

where $\mathscr{E}$ is given by $S\Delta T$=SQ_hR_{th}, where S is the Seebeck coefficient of materials, and R_{el} is the electrical resistance of the TEG. Additionally, R_m is the resistance matching coefficient, defined as $R_m = m/(1+m)^2$, where m represents the ratio of the load resistance to R_{el}. With thinner optimal geometries, an increase in R_{el} reduces η due to a decrease in matching conductance, whereas an increase in R_{th} enhances the conversion factor, leading to a higher η. Furthermore, the geometry can evolve so that the R_m approaches the optimum value of 1/4. Depending on the boundary conditions, TO intelligently balances these trade-offs, optimizing either the conversion factor or the matching conductance to improve overall η (Fig. 2m–o). For example, under weak heating or cooling conditions, TO conceives the thinner geometries to enhance R_{th} and maximize the conversion factor. Conversely, under strong heating or cooling conditions, TO derives thicker geometries to improve matching conductance, as larger ΔT values are naturally created by the boundary conditions (Supplementary Figs. 2, 4, and 6).

The geometric evolution was further influenced by the temperature dependence of material properties. For example, in our model, BiSbTe exhibits a steeper temperature dependence in electrical conductivity (σ) than in thermal conductivity (κ) at low temperatures. This behaviour is also observed in typical TE materials, which exhibit the characteristics of heavily doped semiconductors. Accordingly, changes in R_{el} or the operating temperature range due to geometric evolution were more pronounced than changes in R_{th}. This relation explains the greater η enhancement under weak heating and strong cooling conditions, which shift the operating temperature range to lower values, where the η gain from improved matching conductance outweighs the loss from a reduced conversion factor. Additionally, we examined how variations in the objective function, packaging limit, aspect ratio, load resistance, and contact resistance affect the optimal design (Supplementary discussion and Supplementary Figs. 8 and 9).

Optimums with different materials

We next extended the TO process to a diverse range of materials. Specifically, we incorporated nine different reported material properties into our optimization process under fixed Q_h and convective cooling[19,21,31,40–45]. The selection of these materials was based on their operational temperature ranges, categorized into three groups according to their peak ZT values: low-temperature (300–500 K), mid-temperature (500–700 K), and high-temperature (>700 K) materials (Supplementary Fig. 10a). The optimization process consistently produced an I-shaped configuration across materials, with the final dimensions and proportions varying based on their thermal and electrical properties (Fig. 3a).

Among these, FeNbSb and PbTe exhibited notably high η enhancements, primarily due to their significantly larger ΔT relative to a cuboid and their steep temperature dependence in material properties (Fig. 3b and Supplementary Fig. 10). For instance, the optimal design with PbTe resulted in a 5942% increase in the conversion factor compared to a cuboid (Fig. 3c). This enhancement arose from the larger ΔT and relatively higher averaged ZT at elevated temperatures; for example, in PbTe the optimal design exhibits about six-fold increase in the averaged ZT relative to the cuboid (Supplementary Fig. 11). Meanwhile, the optimal design with FeNbSb increased the conversion factor by 3672% due to its enhanced R_{th}, although the matching conductance was reduced by 67%, leading to a more than tenfold increase in η. In contrast, the optimum design with BiSbTe, AgCuTe, MgAgSb, and Cu_2Se—each exhibiting weaker temperature dependence—showed smaller η enhancements. Nevertheless, η improvements ranging from 9% to 180% were observed in these materials, validating the universal applicability of geometric design for enhancing power generation. Additionally, we performed the same optimization under fixed-T conditions, where efficiency improvements exceeding 200% were achieved (Supplementary discussion and Supplementary Fig. 12).

To gain further insight into how material properties influence optimal geometries, we conducted TO on hypothetical materials by independently varying their κ, σ, and S (Supplementary Fig. 13). Regardless of material properties, TO consistently generated thinner optimal geometries, achieving enhancement in η compared to the cuboid model (Fig. 3d). This enhancement arises from an increase in the conversion factor, driven by a reduction in R_{th} and a corresponding increase in ΔT relative to cuboid models. Specifically, higher κ leads to thinner optimal geometries to sustain larger ΔT. Meanwhile, σ presents a more complex effect: designs with lower σ tend to develop a thicker central region, effectively reducing R_{th} through intelligent geometric shaping. In contrast, a lower S results in an optimized geometry with a thinner height at the top and bottom sections. Overall, these findings suggest that TO effectively balances the trade-off between the conversion factor and matching conductance to maximize η. For instance, a material with low σ can compensate by increasing its cross-sectional area, whereas materials with high κ or low S evolve into thinner geometries to enhance $\mathscr{E}$.

Integrated optimization and experimental validation

Building on these findings, we conducted an integrated optimization for three materials—BiSbTe, PbTe, and Cu_2Se—by incorporating the measured contact resistance values and adjusting the boundary conditions to match their respective properties under fixed Q_h and convective cooling (Fig. 4). The resulting optimized geometries exhibited greater diversity than those obtained in previous cases. In particular, the optimal geometry for PbTe featured a large overall material volume with a distinct thin neck in the mid-lower region, while the optimal geometry for Cu_2Se formed an asymmetric hourglass shape, with more material concentrated near the hot side. To experimentally validate these optimized designs, we fabricated them using a 3D

https://doi.org/10.1038/s41467-026-69901-3

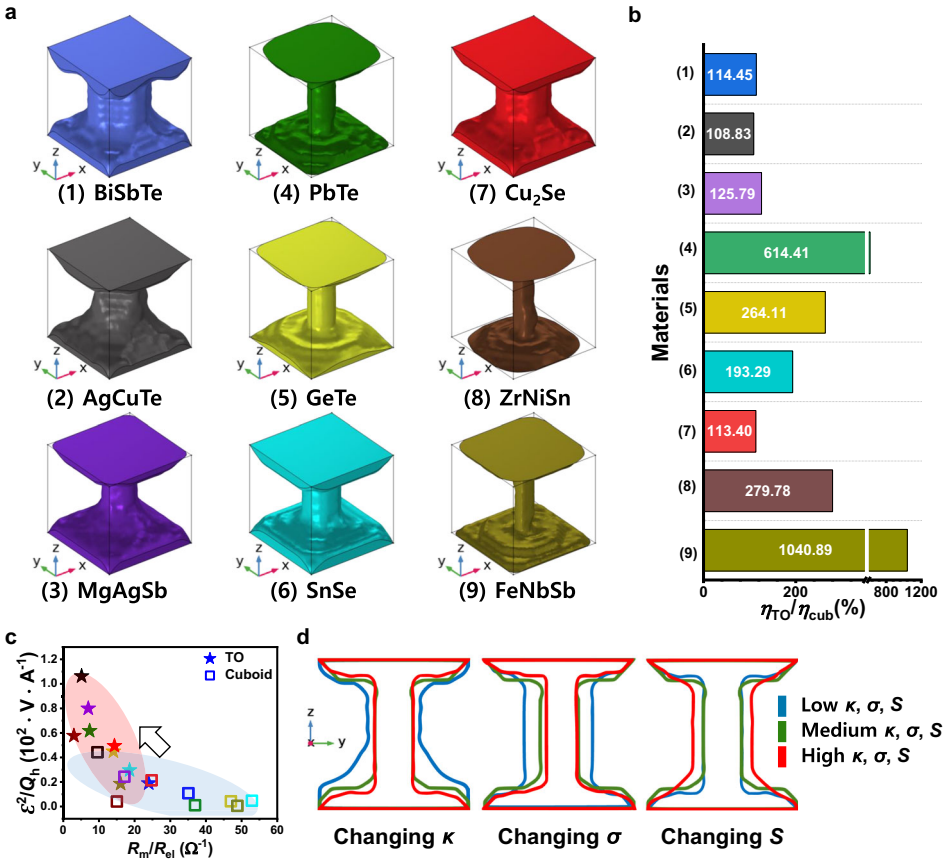

Fig. 3 | Optimums with different materials. a Optimized geometries derived from TO employing nine distinct sets of material properties. **b** η enhancement relative to a cuboid of equivalent material volume from (**a**). **c** Analysis of η enhancement for the optimal designs from (**a**). Star symbols denote the optimized designs, hollow squares denote the reference cuboid, and the colors (in nine variations) match those in (**a**), indicating the corresponding set of material properties. Shaded zones highlight trends for the optimized and cuboid geometries. **d** Side-view outlines of the optimized geometry, representing its shape as seen from the side, under a virtual material model in which k, σ, and S are varied. The baseline properties are $\kappa = 2\ \mathrm{W\,m^{-1}\,K^{-1}}$, $\sigma = 1000\ \mathrm{S\,cm^{-1}}$, and $S = 130\ \mu\mathrm{V\,K^{-1}}$, with $\kappa = 0.4, 2, 10\ \mathrm{W\,m^{-1}\,K^{-1}}$; $\sigma = 100, 1000, 5000\ \mathrm{S\,cm^{-1}}$; and $S = 26, 130, 650\ \mu\mathrm{V\,K^{-1}}$ shown in blue, green, and red, respectively.

printing method (Fig. 4b–d). The geometric fidelity of the printed samples was first confirmed via 3D scanning, revealing dimensional deviation within 10% of the computational models (Fig. 4e–g). For comparison, we also fabricated typical cuboidal TEGs with the same material volume. To evaluate performance, each device was placed between a heater and a water cooler inside a vacuum chamber (Supplementary Fig. 14), where the Q_h, temperatures, and output power were measured.

In all samples, the measured power generation performance closely matched computational predictions for the optimized geometries (Fig. 4h–n). Specifically, BiSbTe achieved a peak η of 5.2%, more than 2.5 times higher than the cuboid's 2%. Likewise, PbTe and Cu_2Se reached peak η values of 5.45% and 5.14%, exceeding their respective cuboid efficiencies by factors of 8.2 and 2. Furthermore, the observed η enhancements at the optimized operating point aligned well with computational predictions, showing increases of 186% for BiSbTe, 626% for PbTe, and 332% for Cu_2Se. These significant improvements arose from several factors, including increased R_{th} and the resulting increase in $\mathscr{E}$, optimized contact areas for fine-tuning R_{el}, and adjustments in R_m. Additional details on measured T and Q_h are provided in Supplementary Figs. 14, 15 and Supplementary Table 1. To further validate our approach, we also examined performance under varying Q_h and T (Supplementary Fig. 16), and in every case, the experimental results for the optimized geometries aligned with simulation predictions, consistently outperforming the conventional cuboid design.

The η of our 3D-printed BiSbTe devices is comparable to or higher than the state-of-the-art performance of TEGs under the same ΔT (Supplementary Fig. 17 and Supplementary Table 2). Unlike BiSbTe, the relatively low η of PbTe- and Cu_2Se-based devices is attributable to a lower ΔT as well as high contact resistances (Supplementary Table 2). Under fixed ΔT and negligible contact resistance, the optimized PbTe- and Cu_2Se-based devices would achieve efficiencies of 9.26% and 11.7%, respectively (Supplementary Fig. 18). These results indicate that the proposed TO framework operates consistently across a broad range of electrical contact resistance levels, and therefore remains applicable as interface quality improves in future device fabrication.

Device-level optimization

To demonstrate TO-based design in the multi-pair module, we extended the TO design framework to compute optimal geometries for one-pair, two-pair, and eight-pair thermoelectric devices comprising p-type BiSbTe and n-type BiTeSe (Supplementary Fig. 19). This model included diffusion barrier layers, solder layers, and ceramic substrates, which are generally incorporated in real devices. Thermal boundary condition was set to a fixed $Q_h = 5{,}000\ \mathrm{W\,m^{-2}}$ with convective cooling on the cold side. Unlike the single-leg optimum, multi-leg designs exhibit geometric asymmetries that arise from lateral heat and current spreading (Fig. 5a). Consistent with resistance–conductance matching, the p-leg is assigned more material than the n-leg to better balance R/K across the pair (Supplementary Fig. 20). Relative to cuboid devices, the TO designed devices achieve 70%, 76%, and 58% η improvements for

https://doi.org/10.1038/s41467-026-69901-3

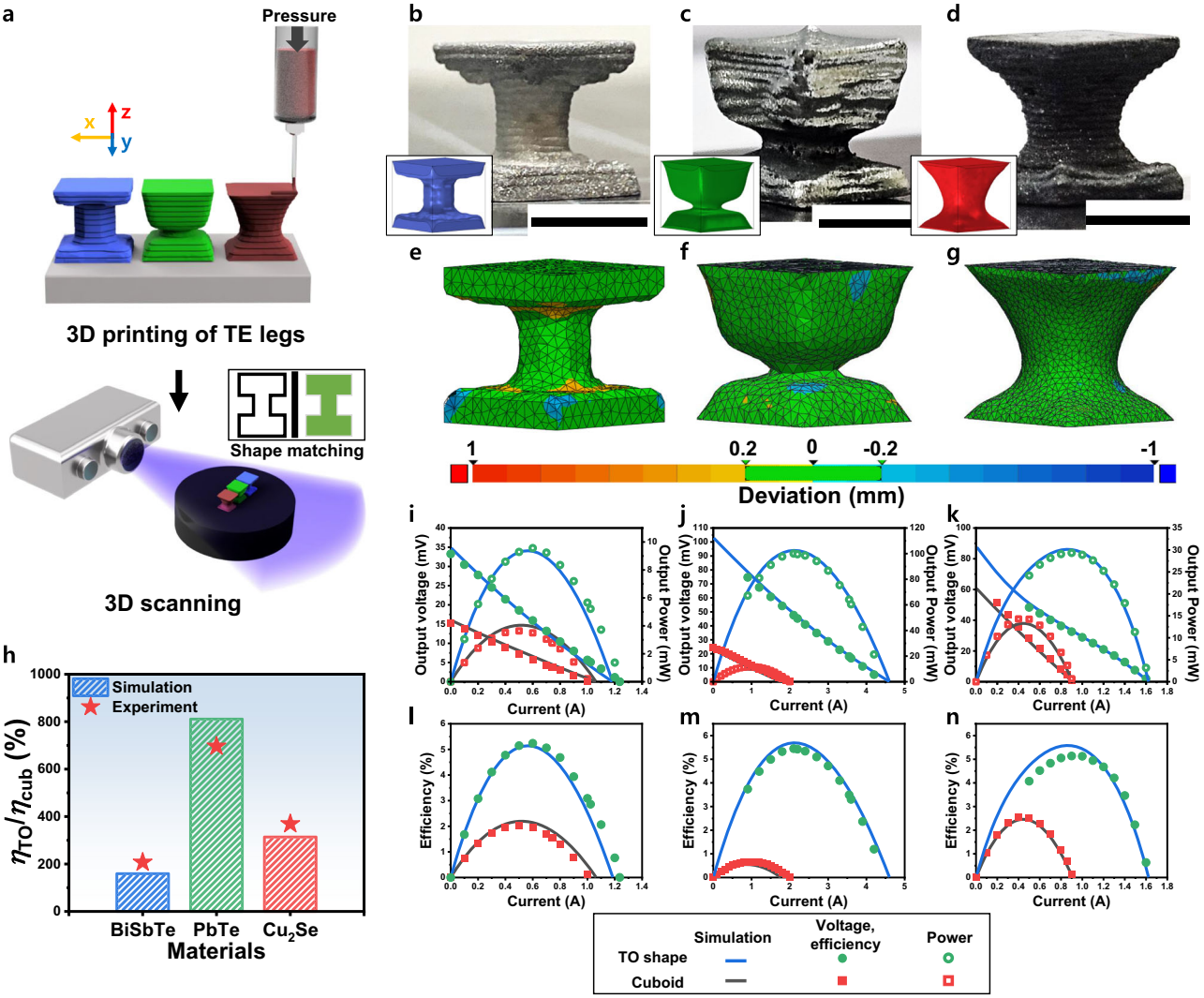

Fig. 4 | Integrated optimization and experimental validation. a Schematic illustrating the 3D printing and scanning processes. Photographs of 3D-printed samples of BiSbTe (**b**), PbTe (**c**), and Cu_2Se (**d**), each featuring an optimized geometry derived from integrated TO. The scale bar is 5 mm. The insets in each panel show the corresponding optimized geometry. 3D scan images corresponding to **b** (**e**), **c** (**f**), and **d** (**g**), respectively. **h** Measured and computationally predicted enhancements in η at the optimized operating condition for each sample, compared with a cuboid of the same material volume. Measured voltage and power (**i**–**k**) and η (**l**–**n**) as a function of current for BiSbTe (**i, l**), PbTe (**j, m**), and Cu_2Se (**k, n**).

the one-, two-, and eight-pair cases, respectively (Supplementary Fig. 21). In addition, we performed TO of a two-pair device under multiple thermal boundary conditions, and the resulting optimized leg geometries exhibit trends consistent with those observed in the single-leg analyses (Supplementary Fig. 22). We further validated the designs by fabricating and testing multi-pair TO and cuboid modules; the measured power and η characteristics closely agree with the simulations (Fig. 5b–d). Additional details on measured T and heat input are provided in Supplementary Fig. 23. Also, long-term operation and thermal-cycling tests on the optimized two-pair modules proved thermal stability (Supplementary Fig. 24).

We further conducted the TO framework to generate optimal geometries across multiple types of devices—planar, tubular, and Y-shaped (Fig. 5a). Instead of starting from a fixed shape, the optimizer operates on the full design domain, producing an unintuitive geometry tailored to the imposed system condition.

Mechanical stability of TE device is essential for long-term, application-level viability. To assess this explicitly, we evaluated the failure strength of BiSbTe cuboid and optimized legs via uniaxial compression (Supplementary Fig. 25). The optimized leg shows a larger engineering strain before macroscopic failure than the cuboid. This is primarily attributed to its non-uniform geometry, which promotes deformation localization and progressive damage accumulation near the compliant neck region. The further details were described in the Supplementary Discussion. To further, we incorporated the compressive stress as an additional constraint into a TO process for the two pairs-device (Supplementary Fig. 26). The TO process generates a geometry that satisfies the stress upper limit of the industrial standard (1.2 MPa)[46], while preserves high efficiency. This co-design capability, which balances requirements such as mechanical robustness and thermoelectric performance within a single unified formulation, is a key strength of TO.

Discussion

Our study demonstrates that TO can systematically generate optimal geometries for TE materials, maximizing power generation efficiency under diverse boundary conditions and material properties. This approach reveals universal design strategies for enhancing η. Under varying thermal conditions, TO consistently produces distinct geometric features, including a pronounced I-shape or an asymmetric

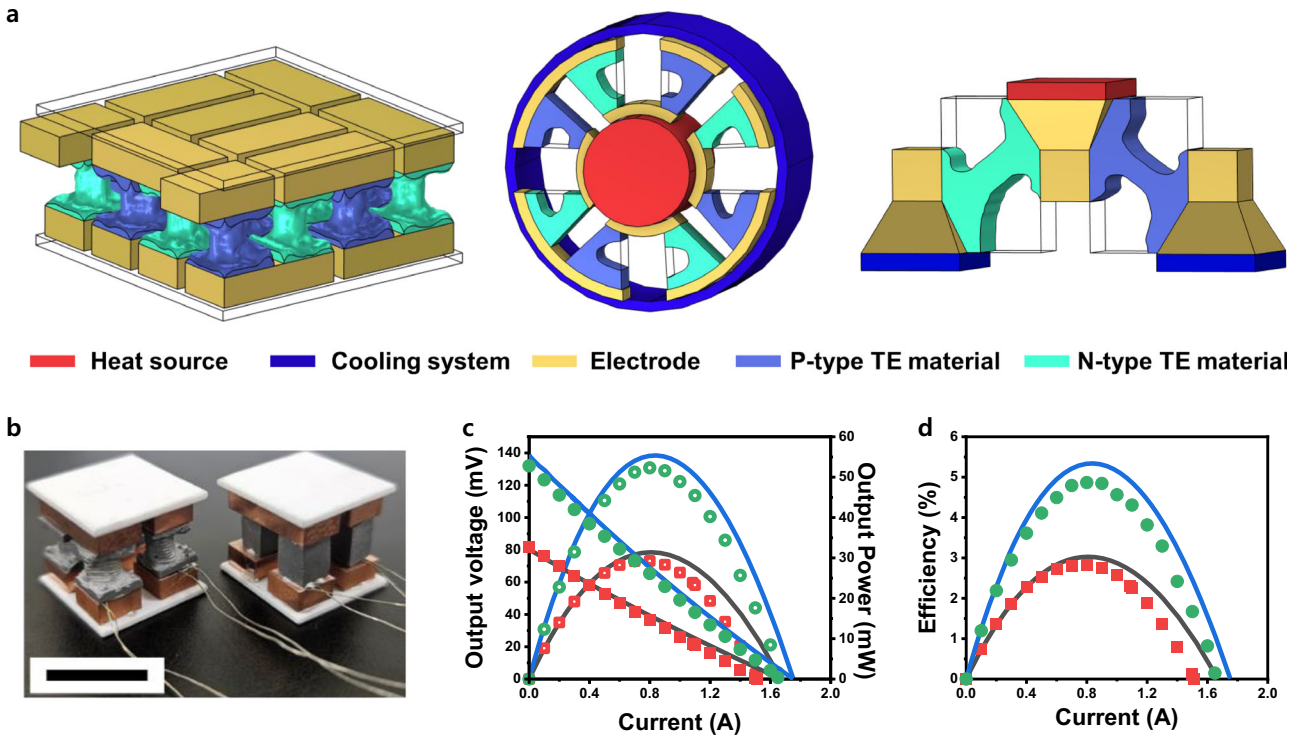

Fig. 5 | Device-level optimization and experimental validation. a Various types of optimal TEG, such as planar, tubular and Y-shaped types. **b** Photograph of 3D-printed optimal geometry- and cuboid-based two-pair TEGs. Measured voltage and power (**c**) and η (**d**) as a function of current.

hourglass structure, by balancing the conversion factor and matching conductance. Furthermore, intrinsic material properties interact with geometry, influencing efficiency gains. Materials with steep temperature-dependent properties exhibit significant η enhancements through geometric adaptation, whereas those with inherently low κ yield only marginal improvements. Experimental validation with 3D-printed materials and their multi-pair modules confirms the feasibility and effectiveness of our computationally derived designs. These findings emphasize the fundamental role of geometry in reconciling imbalances between electrical and thermal transport properties induced by material characteristics. The scalability of our TO framework—applicable across diverse boundary conditions, heterogeneous materials, and multi-objective optimization problems—suggests its potential for revolutionizing high-efficiency TE devices. Ultimately, this approach can drive advancements in a broad range of energy-harvesting technologies.

Methods

Materials

Elemental granules of Bi, Sb, Se, and Te (99.999%) were purchased from 5 N Plus. Elemental Pb (99.95%) and Cu (99.9%) were purchased from Alfa Aesar. Elemental Na (>95%) was purchased from Aldrich Chemical. Isopropanol (99.5%) and Se (99.999%) powder for the synthesis of Se polyanion from Samchun Chemicals and Alfa Aesar, respectively. Ethanethiol (>97%), ethylenediamine (>99.5%), acetonitrile (>99.8%), and glycerol (>99.5%) were purchased from Aldrich Chemical.

Topology optimization

We employ a density-based TO approach to systematically design TEGs with enhanced power generation efficiency. This method redistributes material within a predefined design domain to optimize performance. The design problem is formulated as a mathematical optimization problem, maximizing either power generation (P) or η for a given constraint:

$$\max f(V,T;\rho) = P(V,T;\rho) or\ \eta(V,T;\rho) \tag{2}$$

subject to

$$V_{TE} \le V_c$$

$$0 \le \rho_i \le 1 (i = 1 \ldots n) \tag{3}$$

$$\mathbf{R}(V,T) = 0$$

Where the state variables $V(\Omega)$ and $T(\Omega)$ are the electric potential and temperature field defined in the design domain Ω, respectively. V_{TE} corresponds to the volume of material used, and V_c represents the maximum allowable volume. **R** represents the residual of the governing equation formulated via the Galerkin method. These are solved by finite element analysis utilizing quadratic Lagrange hexahedron elements for accurate spatial resolution. The ρ_i is a mathematical design variable ranging from 0 to 1 to represent material existence within the element of index i. The objective function $f(\rho)$, either P or η, reads:

$$P = \int_{\Omega_l} \mathbf{J} \cdot \mathbf{E} d\Omega,\ \eta = \frac{P}{Q_h} = \frac{\int_{\Omega_l} \mathbf{J} \cdot \mathbf{E} d\Omega}{\int_{\Omega_{TE}} \mathbf{q} \cdot \mathbf{n} d\Omega} \tag{4}$$

The governing physics of the TO framework couples thermal and electrical transport equations, which describe steady-state heat conduction, electrical potential distribution, and thermoelectric effects:

$$\nabla \cdot \mathbf{q} + \mathbf{J} \cdot \mathbf{E} = 0 \tag{5}$$

$$\nabla \cdot \mathbf{J} = 0$$

where **q** is the heat flux, **J** is the electric current density, and **E** is the electric field intensity. These equations are coupled through the Seebeck effect, which relates the generated voltage to the temperature gradient:

$$\mathbf{J}(V,T,x) = \sigma(\rho)(E - S(\rho)\nabla T) \tag{6}$$

$$\mathbf{q}(V,T,x) = S(\rho)T\mathbf{J} - \kappa(\rho)\nabla T$$

To represent the material properties with varying density ρ, we utilize the Solid Isotropic Material with Penalization (SIMP) method that is of wide use in engineering applications due to its computational efficiency and ease of implementation[47,48]:

$$\Xi(x,\rho) = \Xi_0\left(\rho_\epsilon + (1-\rho_\epsilon)\rho^p\right) \tag{7}$$

where Ξ represents material property (i.e., σ, S, κ) and Ξ_0 is the intrinsic material properties measured through experiments, respectively. The ρ_ϵ is small real value that prevents numerical instability, and p is the penalty parameter, which was set to 3. For millimetre-scale legs, surface-to-ambient radiation removes only a few percent of the heat that enters through the hot junction. We assumed that radiation was ignored for improved computational efficiency

To improve computational stability and manufacturability, numerical techniques such as the Helmholtz filter and hyperbolic tangent projection with parameter continuation are applied to control minimum feature sizes and avoid checkerboarding artifacts[49,50]. The projection slope β is raised from 1 to β_{max}, which was set to at least 100 (Supplementary Fig. 27). A Helmholtz filter of radius $r = 1.5\,h_e$ (h_e = element size) was enforced throughout to guarantee printable feature resolution. The optimization process is iteratively solved using the adjoint sensitivity method and the Method of Moving Asymptotes (MMA), ensuring convergence toward optimal solutions[51].

Upon convergence, the optimized material distribution is post-processed as a volumetric field, and a solid-void interface is extracted at a 50% density threshold to generate physically realizable geometries suitable for fabrication. R_{el}, ΔT, output voltage, output power, and η of the optimized and reference TE generator were computed based on the final optimized design, accounting for the influence of material density variations. All numerical procedures, including finite element analysis, sensitivity analysis, and optimization processes, were executed within the commercial software COMSOL Multiphysics, which was complemented by Matlab Livelink for the post-process and the sensitivity filtering.

TEG models

To systematically evaluate topology optimization across different system parameters, including thermal boundary conditions, material properties, and contact resistance, a standardized TEG model is established as shown in Fig. 1a.

Each TEG consists of a TE material positioned between two copper electrodes. Initially, the TE region is designed as a cuboid measuring $6 \times 6 \times 6\ mm^3$, while the copper electrodes are $6 \times 6 \times 3\ mm^3$. The TE domain is discretized into approximately 8000 finite elements to ensure high-resolution optimization.

Regarding input data for the optimization, we employed temperature-dependent thermoelectric properties from the literature for each material system. In the case of BiSbTe, PbTe, and Cu_2Se, we performed measurements and found no significant deviations from the reported datasets (Supplementary Fig. 28). Also, we further checked a 3D-printed BiSbTe single sample by measuring heat flux along three orthogonal directions to check anisotropy" (Supplementary Fig. 29).

The boundary conditions for the TEG models are carefully defined to reflect realistic operational environments. All side surfaces are treated as adiabatic and electrically insulated. The top electrode functions as the hot side with an electrical ground, while the bottom electrode serves as the cold side, connected to an external load resistance of R_L to facilitate power generation. Additionally, contact resistivity at the TE-electrode interface is incorporated into the model, with values obtained from experimental measurements. In the integrated optimization, the convection coefficient was set to $h = 1200\ W\,m^{-2}\,K^{-1}$, a value measured using a BiSbTe cuboid device (Supplementary Fig. 30).

To assess the effects of different thermal boundary conditions, TO is conducted using BiSbTe properties under a range of thermal environments. The first set of simulations examines convective heating and cooling, varying the h from 10 to $1000\ W\,m^{-2}\,K^{-1}$, while the ambient temperatures are fixed to 450 K on the hot side and 293.15 K on the cold side. Another set of scenarios involves applying a fixed heat flux to the hot side, with heat flux values of 5000, 7500, and $10000\ W\,m^{-2}$, while maintaining convective cooling on the cold side (Supplementary Fig. 3). In addition, a series of optimizations explore conditions where the hot-side temperature is held constant, and varying cooling fluxes are applied to ensure the device operates within the thermal stability range of the materials. To ensure the material operates within the valid range, a minimum temperature of 323.15 K was enforced to ensure realistic operating conditions for the TE device (Supplementary Fig.4).

The influence of material properties is also evaluated by applying topology optimization to nine different thermoelectric materials, including BiSbTe, PbTe, Cu_2Se, and FeNbSb. These materials are selected to cover a broad range of temperature-dependent electrical and thermal characteristics. The boundary conditions were set such that the hot side received a constant heat flux of $10{,}000\ W\,m^{-2}$ while convective cooling was applied with a convection coefficient of $1200\ W\,m^{-2}\,K^{-1}$ and an ambient temperature of 293.15 K. The optimizations with virtual materials were conducted under the same system conditions.

Additionally, to perform optimizations examining variations in contact resistance, aspect ratio, and load resistance, a common boundary condition was adopted: a constant heat flux of $5000\ W\,m^{-2}$ was supplied from the hot side, with convective cooling characterized by a convection coefficient of $1200\ W\,m^{-2}\,K^{-1}$ and an ambient temperature of 293.15 K. The optimal design according to the objective function was performed under fixed conditions of hot side temperature of 450 K and cold side temperature of 323.15 K.

In the integrated design, a constant heat flux was supplied according to each material's properties. Specifically, a heat flux of $5000\ W\,m^{-2}$ was applied for BiSbTe, $50000\ W\,m^{-2}$ for PbTe and $15000\ W\,m^{-2}$ for Cu_2Se. In all cases, convective cooling was maintained with a convection coefficient of $1200\ W\,m^{-2}\,K^{-1}$ and an ambient temperature of 293.15 K. Additionally, the maximum hot-side temperatures were set to 750 K for PbTe and 800 K for Cu_2Se. The contact resistance was assigned based on the measured values at the interface between each material and the electrodes (Supplementary Fig. 1).

Device-level TO was performed using models that explicitly include diffusion barrier layers, solder layers, and ceramic substrates for one-pair, two-pair, and eight-pair systems. For the diffusion barrier, nickel properties were used, and the barrier thickness was set to 10 μm. The solder layer was modelled with a thickness of 50 μm. These models were constructed by increasing the overall device size and total TE material quantity with the pair number.

Conversion factor and matching conductance

The energy-conversion efficiency of a TEG is defined as

$$\eta = \frac{P}{Q_h} \tag{8}$$

where the electrical power delivered to the load is

$$P = \frac{V^2}{R_{load}} = \frac{\mathscr{E}^2 R_{load}}{(R_{el} + R_{load})^2} \tag{9}$$

where V is closed-circuit voltage. Introducing the matching ratio ($m = R_{load}/R_{el}$), the power can be written as

$$P = \frac{\mathscr{E}^2 m}{(1+m)^2 R_{el}} \tag{10}$$

Substituting this expression into the efficiency definition gives

$$\eta = \frac{\mathscr{E}^2}{Q_h} \frac{R_m}{R_{el}} \tag{11}$$

Synthesis of viscoelastic TE inks

TE powders for both BiSbTe and Na-doped PbTe were synthesized using the same high-energy ball milling process with a Monomill (Pulverisette 6, Fritsch) for 11 h. An 80 ml zirconia milling jar with 5 mm zirconia grinding balls was used at a ball-to-powder weight ratio of 5:1. Milling for both BiSbTe ($Bi_{0.55}Sb_{1.45}Te_3$) and Na-doped PbTe ($Pb_{0.98}Na_{0.02}Te$) was conducted at 450 rpm. To synthesize Cu_2Se, elemental Cu and Se powders were ball-milled in a ball miller (8000 M Mixer/Mill, SPEX) for 200 min and subsequently sieved to remove particles larger than 45 μm. For the BiSbTe ink, a Sb_2Te_4 ChaM binder was synthesized by dissolving 0.64 g of antimony powder and 1.36 g of tellurium powder in a co-solvent comprising 4 mL of ethanethiol and 16 mL of ethylenediamine in a nitrogen-filled glove box. After stirring for over 24 h until the solution turned dark purple, 40 mL of acetonitrile was added to precipitate the binder via centrifugation at 7,500 rpm for 10 min, and the precipitate was then dried under vacuum for 30 min. This binder was mixed with 4 g of BiSbTe powder and 4 g of glycerol using a planetary centrifugal mixer (ARM-100, Thinky) for 2 h to yield a homogeneous ink. For the PbTe ink, the TE powder was combined with 0.5 wt% tellurium powder and dispersed in glycerol, with the glycerol mass set to half that of the total powder. The mixture was then homogenized for 1 h in the planetary centrifugal mixer. For the Cu_2Se ink, a Se polyanion additive was first prepared by dissolving 0.5 g of selenium powder in 0.5 mL of ethanethiol and 4.5 mL of ethylenediamine at room temperature with vigorous stirring for 72 h. Five millilitres of this solution were mixed with 37.5 mL of isopropanol and centrifuged at 7,715 g for 10 min to precipitate the Se polyanion, which was then vacuum-dried for 1 h. Finally, 2–3 g of ball-milled Cu_2Se powder and 1–1.5 g of the dried Se polyanion were dispersed in 2.5 g of glycerol and mixed for 2 h in the planetary centrifugal mixer to produce the final ink.

3D printing of TE materials

3D printing was performed using a home-built, extrusion-based printer equipped with programmable pressure controls. The synthesized ink was loaded into a 5 ml syringe (Saejong) fitted with a metal nozzle having an inner diameter of 340 μm. The printing process was carried out at room temperature with a 1 s interval between layer depositions. The as-printed sample was then dried at 423 K for over 12 h and subsequently annealed under a nitrogen atmosphere under different conditions: BiSbTe was annealed at 723 K for 2 h; PbTe underwent a two-step annealing at 1073 K for 2 h followed by 923 K for 3 h; and Cu_2Se was annealed at 1233 K for 13 h.

3D scanning of TE materials

Conformity between the 3D-printed samples and the design drawings was assessed using a 3D scanner (Gom Scan, Zeiss) employing a non-contact optical measurement technique (fringe projection with a blue LED). The resulting STL files were analyzed for congruence using the commercial software Control X.

Fabrication and power measurement of TE device

The printed samples were attached to Cu electrodes using SAC solder paste at 250 °C for BiSbTe, Ni–Sn paste at 450 °C for PbTe, and silver paste (Pyro-Duct 597-A, Aremco) for Cu_2Se. Output power was measured under a controlled temperature difference using a ceramic heater as the heat source and a water-circulating chiller for cooling, while K-type thermocouples connected to a Keithley 2000 multimeter monitored the temperature changes. To prevent unintended oxidation and air convection, all evaluations were performed within a vacuum chamber.

Data availability

All data generated or analyzed during this study are included in the published article and its Supplementary Information. The source data underlying the figures of the Main Text are provided within the "Source Data" file. Source data are provided with this paper.

Code availability

The COMSOL Multiphysics codes generated for this work have been uploaded to a public repository at https://doi.org/10.5281/zenodo.18410821.

References

1. Munch, E. et al. Tough, bio-inspired hybrid materials. *Science* **322**, 1516–1520 (2008).
2. Tian, Y. et al. Adhesion and friction in gecko toe attachment and detachment. *Proc. Natl. Acad. Sci. USA* **103**, 19320–19325 (2006).
3. Berger, J., Wadley, H. & McMeeking, R. Mechanical metamaterials at the theoretical limit of isotropic elastic stiffness. *Nature* **543**, 533–537 (2017).
4. Baba, T. Slow light in photonic crystals. *Nat. Photonics* **2**, 465–473 (2008).
5. Ahmed, H. E., Salman, B. H., Kherbeet, A. S. & Ahmed, M. Optimization of thermal design of heat sinks: a review. *Int. J. Heat. Mass Transf.* **118**, 129–153 (2018).
6. Bendsøe, M. P. & Sigmund, O. *Topology Optimization: Theory, Methods, and Applications* (Springer, 2013).
7. Bendsøe, M. P. & Kikuchi, N. Generating optimal topologies in structural design using a homogenization method. *Comput. Methods Appl. Mech. Eng.* **71**, 197–224 (1988).
8. Aage, N., Andreassen, E., Lazarov, B. S. & Sigmund, O. Giga-voxel computational morphogenesis for structural design. *Nature* **550**, 84–86 (2017).
9. Cavazzuti, M. et al. High performance automotive chassis design: a topology optimization based approach. *Struct. Multidiscip. Optim.* **44**, 45–56 (2011).
10. Chen, C.-T., Chrzan, D. C. & Gu, G. X. Nano-topology optimization for materials design with atom-by-atom control. *Nat. Commun.* **11**, 3745 (2020).
11. Liu, Y. et al. Ultrastiff metamaterials generated through a multilayer strategy and topology optimization. *Nat. Commun.* **15**, 2984 (2024).
12. Kobayashi, H. et al. Computational synthesis of locomotive soft robots by topology optimization. *Sci. Adv.* **10**, eadn6129 (2024).

13. Sundaram, S., Skouras, M., Kim, D. S., van den Heuvel, L. & Matusik, W. Topology optimization and 3D printing of multimaterial magnetic actuators and displays. *Sci. Adv.* **5**, eaaw1160 (2019).
14. DiSalvo, F. J. Thermoelectric cooling and power generation. *Science* **285**, 703–706 (1999).
15. Bell, L. E. Cooling, heating, generating power, and recovering waste heat with thermoelectric systems. *Science* **321**, 1457–1461 (2008).
16. Snyder, G. J. & Toberer, E. S. Complex thermoelectric materials. *Nat. Mater.* **7**, 105–114 (2008).
17. He, J. & Tritt, T. M. Advances in thermoelectric materials research: looking back and moving forward. *Science* **357**, eaak9997 (2017).
18. Biswas, K. et al. High-performance bulk thermoelectrics with all-scale hierarchical architectures. *Nature* **489**, 414–418 (2012).
19. Choo, S. et al. Geometric design of Cu_2Se-based thermoelectric materials for enhancing power generation. *Nat. Energy* **9**, 1105–1116 (2024).
20. Kim, K. et al. Heat-dissipation design and 3D printing of ternary silver chalcogenide-based thermoelectric legs for enhancing power generation performance. *Adv. Sci.* **11**, 2402934 (2024).
21. Lee, J. et al. Doping-induced viscoelasticity in PbTe thermoelectric inks for 3D printing of power-generating tubes. *Adv. Energy Mater.* **11**, 2100190 (2021).
22. Karthikeyan, V. et al. Three dimensional architected thermoelectric devices with high toughness and power conversion efficiency. *Nat. Commun.* **14**, 2069 (2023).
23. Choo, S. et al. Cu_2Se-based thermoelectric cellular architectures for efficient and durable power generation. *Nat. Commun.* **12**, 3550 (2021).
24. Fabián-Mijangos, A., Min, G. & Alvarez-Quintana, J. Enhanced performance thermoelectric module having asymmetrical legs. *Energy Convers. Manag.* **148**, 1372–1381 (2017).
25. Zhang, Q. et al. Realizing a thermoelectric conversion efficiency of 12% in bismuth telluride/skutterudite segmented modules through full-parameter optimization and energy-loss minimized integration. *Energy Environ. Sci.* **10**, 956–963 (2017).
26. Qiu, P. et al. High-efficiency and stable thermoelectric module based on liquid-like materials. *Joule* **3**, 1538–1548 (2019).
27. He, Z.-Z. A coupled electrical-thermal impedance matching model for design optimization of thermoelectric generator. *Appl. Energy* **269**, 115037 (2020).
28. Yang, W. et al. Performance improvement and thermomechanical analysis of a novel asymmetrical annular thermoelectric generator. *Appl. Therm. Eng.* **237**, 121804 (2024).
29. Weng, Z. et al. Performance improvement of variable-angle annular thermoelectric generators considering different boundary conditions. *Appl. Energy* **306**, 118005 (2022).
30. Zhu, W. et al. Theoretical analysis of shape factor on performance of annular thermoelectric generators under different thermal boundary conditions. *Energy* **239**, 122285 (2022).
31. Yang, S. E. et al. Composition-segmented BiSbTe thermoelectric generator fabricated by multimaterial 3D printing. *Nano Energy* **81**, 105638 (2021).
32. Van Erp, R., Soleimanzadeh, R., Nela, L., Kampitsis, G. & Matioli, E. Co-designing electronics with microfluidics for more sustainable cooling. *Nature* **585**, 211–216 (2020).
33. Zou, K. et al. Electronic cooling and energy harvesting using ferroelectric polymer composites. *Nat. Commun.* **15**, 6670 (2024).
34. Gebrael, T. et al. High-efficiency cooling via the monolithic integration of copper on electronic devices. *Nat. Electron.* **5**, 394–402 (2022).
35. Kraemer, D. et al. High-performance flat-panel solar thermoelectric generators with high thermal concentration. *Nat. Mater.* **10**, 532–538 (2011).
36. Kang, J. S. et al. Integration of boron arsenide cooling substrates into gallium nitride devices. *Nat. Electron.* **4**, 416–423 (2021).
37. Baranowski, L. L., Snyder, G. J. & Toberer, E. S. Concentrated solar thermoelectric generators. *Energy Environ. Sci.* **5**, 9055–9067 (2012).
38. Liu, Z. et al. Maximizing the performance of n-type Mg_3Bi_2-based materials for room-temperature power generation and thermoelectric cooling. *Nat. Commun.* **13**, 1120 (2022).
39. El Oualid, S. et al. Innovative design of bismuth-telluride-based thermoelectric micro-generators with high output power. *Energy Environ. Sci.* **13**, 3579–3591 (2020).
40. Jiang, J. et al. Achieving high room-temperature thermoelectric performance in cubic AgCuTe. *J. Mater. Chem. A* **8**, 4790–4799 (2020).
41. Zhang, X. et al. High-performance $MgAgSb/Mg_3(Sb, Bi)_2$-based thermoelectrics with $\eta = 12\%$ at $T \leq 583$ K. *Joule* **8**, 3324–3335 (2024).
42. Perumal, S. et al. Realization of high thermoelectric figure of merit in GeTe by complementary co-doping of Bi and In. *Joule* **3**, 2565–2580 (2019).
43. Zhao, L.-D. et al. Ultrahigh power factor and thermoelectric performance in hole-doped single-crystal SnSe. *Science* **351**, 141–144 (2016).
44. Yang, X. et al. Enhancement in thermoelectric properties of ZrNiSn-based alloys by Ta doping and Hf substitution. *Acta Mater.* **233**, 117976 (2022).
45. Fu, C. et al. Realizing high figure of merit in heavy-band p-type half-Heusler thermoelectric materials. *Nat. Commun.* **6**, 8144 (2015).
46. TE Technology, Inc. Thermoelectric module (TEM) peltier element mounting procedure. https://tetech.com/wp-content/uploads/2013/11/tem_thermoelectric_module_mounting_procedure.pdf (2025).
47. Bendsøe, M. P. Optimal shape design as a material distribution problem. *Struct. Optim.* **1**, 193–202 (1989).
48. Rozvany, G. I., Zhou, M. & Birker, T. Generalized shape optimization without homogenization. *Struct. Optim.* **4**, 250–252 (1992).
49. Lazarov, B. S. & Sigmund, O. Filters in topology optimization based on Helmholtz-type differential equations. *Int. J. Numer. Methods Eng.* **86**, 765–781 (2011).
50. Guest, J. K., Prévost, J. H. & Belytschko, T. Achieving minimum length scale in topology optimization using nodal design variables and projection functions. *Int. J. Numer. Methods Eng.* **61**, 238–254 (2004).
51. Svanberg, K. The method of moving asymptotes—a new method for structural optimization. *Int. J. Numer. Methods Eng.* **24**, 359–373 (1987).

Acknowledgements

This research was supported by the Mid-Career Researcher Program (RS-2022-NR070604) and Nano & Material Technology Development Program (RS-2024-00449743) through the National Research Foundation of Korea (NRF) funded by the Ministry of Science and ICT.

Author contributions

J.L., S.E.Y., and S.C. contributed equally to this work. J.L., S.E.Y., S.C., H.C., and J.S.S. designed the experiments, analysed the data, and wrote the paper. J.L., H.L., and H.C. performed the topology optimization studies. J.L., S.E.Y., S.C., H.H., K.K., and Y.E.P. carried out the fabrication and measurement of the devices. J.L., H.H.L., and D.W.S. performed the mechanical durability tests and analysed the results. All authors discussed the results and commented on the manuscript.

Competing interests

The authors declare no competing interests.

Additional information

Supplementary information The online version contains supplementary material available at https://doi.org/10.1038/s41467-026-69901-3.

Correspondence and requests for materials should be addressed to Hayoung Chung or Jae Sung Son.

Peer review information *Nature Communications* thanks the anonymous reviewer(s) for their contribution to the peer review of this work. A peer review file is available.